



Research on the Influence of Inflow Conditions on the Aerodynamic Performance of a Tandem Cascade

Z. Yang, B. Liu, X. Mao[†], B. Zhang and H. Wang

School of Power and Energy, Northwestern Polytechnical University, Xi'an, Shaanxi, 710072, P. R. China

[†]Corresponding Author Email: maoxiao_chen@nwpu.edu.cn

(Received March 25, 2022; accepted July 8, 2022)

ABSTRACT

We perform a thorough numerical analysis of the impact of inflow conditions on the aerodynamic performance of a tandem cascade. In particular, we investigate the effects of the incidence angle and the inlet boundary layer (IBL) thickness on the three-dimensional flow field structure and aerodynamic performance. Our results show that the gap flow strength of the tandem cascade decreases with the increase of incidence angle, and it can effectively reduce the mixing of the wakes of the forward blade (FB) and rear blade (RB). In turn, this prevents the passage vortex (PV) in the RB passage from developing along the circumferential direction. The occurrence of IBL does not modify the effects of the incidence angle on the tandem cascade, however, it reduces the load of the RB and the gap flow strength near the endwall. Under all incidence angles, IBL increases the total pressure loss of the tandem cascade, and decreases the static pressure rise (except for an incidence angle equal to -6°). The maximum loss increment is at 2° incidence angle, and the maximum static pressure rise decrement is at 6° incidence angle (Thick-IBL condition) or 7° incidence angle (Thin-IBL condition). Furthermore, we found that the presence of IBL changes the minimum loss condition from 0° (design condition) to -2° incidence angle. Our results thus indicate that in the practical engineering application of the tandem cascade, the reality that IBL degrades the tandem cascade performance in the full incidence angle range should be considered. And the strong endwall secondary flow effect caused by IBL should be considered in the tandem cascade three-dimensional design, so that the tandem cascade two-dimensional performance advantage can be better played.

Keywords: Tandem cascade; Inlet boundary layer; Total pressure loss; Corner separation; Compressor.

NOMENCLATURE

3D	three-dimensional	PIV	induced vortex of passage vortex
AO	Axial Overlap	PS	Pressure Surface
C_a /(mm)	axial chord length	PV	Passage Vortex
C_p	static pressure rise coefficient	$Q/(s^{-2})$	vortex determination criterion
CR	Chord Ratio	RB	Rear Blade
CV	Corner Vortex	SS	Suction Surface
FB	Forward Blade	SST	Shear Stress Transport
i /(degree)	incidence angle	SSV	suction surface separation vortex
IBL	Inlet Boundary Layer	TR	camber ratio
KBB/(degree)	Rear blade approximate incidence angle	TSV	trailing-edge shedding vortex
LE	Leading Edge	TE	Trailing Edge
p_1 /(Pa)	inlet static pressure	y^+	non-dimensional wall distance
p /(Pa)	local static pressure	ω	total pressure loss coefficient
P_{t1} /(Pa)	inlet total pressure	$\Omega_z/(s^{-1})$	axial vorticity
P_t /(Pa)	local total pressure	β_2 /(degree)	outflow angle
PP	Percent Pitch		

1. INTRODUCTION

Increasing the pressure diffusion capacity of a compressor is one of the effective ways to improve the thrust-to-weight ratio of an aeroengine. However, the increase of pressure diffusion capacity will often

lead to the increase of the axial adverse pressure gradient and the circumferential pressure gradient of the blade passage, thereby exacerbating the corner separation. In fact, large-scale corner separation causes serious passage blockage and total pressure

loss (Mao *et al.* 2018; Wang *et al.* 2020), which greatly reduces the working stability of compressors. In order to improve compressor performance, recent studies have shown that tandem blades have the advantages of large flow turning angle, low total pressure loss, and wide working range (Ju and Zhang 2010; Hoeger *et al.* 2011; Eshraghi *et al.* 2016). As shown in Fig. 1, the control principle of tandem blades is based on the fact that the gap flow between the forward blade (FB) and rear blade (RB) accelerates the high-energy incoming flow from FB, and guides it to the suction surface of the RB, and blowing away the low-energy area of the FB wake. The new boundary layer is then formed again on the leading edge of the RB. The re-formation of the boundary layer prevents the development of the boundary layer separation (McGlumphy 2008).

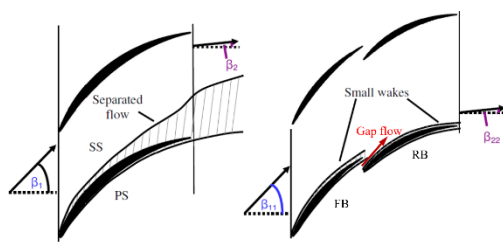


Fig. 1. Comparison of two-dimensional flow characteristics between single blade and tandem blades by McGlumphy.

Earlier researches on tandem blades mostly focused on the overall performance of single-stage or multi-stage tandem compressors (Bammert and Staude 1980; Wennerstrom 1990). In the recent years, Roy *et al.* (2009) has investigated behaviour of the tandem structure applied to the partial blade height of a compressor rotor, and the aerodynamic performance of the compressor has been significantly improved. Liu *et al.* (2021) changed the rotor and stator of a single-stage compressor to the tandem structure, and experiments have proved that the tandem design significantly improves the compressor load and efficiency.

In recent years, research on the design of tandem blades has been mainly devoted to the position arrangement and the loading ratio assignment of the FB and RB. Many studies have shown that a high percent pitch (PP) and low axial overlap (AO) are convenient choices, and that a loading ratio of about 1 is the most appropriate (McGlumphy *et al.* 2009; McGlumphy *et al.* 2010). Following these findings, the tandem blade in this article has been designed accordingly. The loading ratio of the FB and RB is set about 1 by adjusting the camber ratio (TR) and chord ratio (CR) of the FB and RB.

Following the development of experimental technique and computational fluid dynamics, secondary flow effect in three-dimensional (3D) corner region of tandem cascade have become an important research field. McGlumphy *et al.* (2010) studied the corner separation phenomenon of tandem cascade by means of numerical simulations. They

found that the FB aerodynamic characteristics are similar to those of conventional single-row rotor, such that the endwall area generated significant corner separation under the influence of secondary flow at the near-stall condition. The RB flow was affected by the FB outlet flow, and the low-energy fluid merged with the FB wake, causing a non-uniform flow in the blade height direction. The experiments of Hertel *et al.* (2014) on oil flow confirmed McGlumphy's conclusion. As the incidence angle increased, the flow topology in the FB corner region changed in a way similar to what could be observed in a conventional compressor cascade. The RB separation range decreased with increasing incidence angle. In addition, due to the jet effect of the FB wake, the development of the secondary flow from the RB endwall to suction surface was inhibited. Tesch *et al.* (2014) obtained results similar to those of Hertel in cascade outlet loss contours and oil flow streamlines.

More recently, intelligent optimization design methods have been employed in tandem blade design (Schlaps *et al.* 2014; Cheng *et al.* 2017; Song *et al.* 2019). In addition, tandem cascades have been combined with other flow control methods (endwall boundary layer suction, non-axisymmetric endwall profiling, etc.) to control the 3D corner separation, and achieved good effect (Zhang *et al.* 2019; Cao *et al.* 2021).

Inlet conditions (Mach number, incidence angle, turbulence, and boundary layer thickness, etc.) have a relevant impact on the aerodynamic performance of compressor blades. In particular, the endwall boundary layer plays a key role in the formation of secondary flow and corner separation. In turn, the influence of inlet boundary layer (IBL) thickness on compressor stages or cascades received large attention. In the 1980s, Wagner *et al.* (1985a, 1985b) carried out a study on the IBL influence on the interaction effect between the rotor blades of an axial compressor and the passage flow characteristics. Choi *et al.* (2011) studied the influence of the IBL thickness on the rotating stall of a compressor rotor. The results have shown that the rotating stall of the thin IBL condition occurred at a lower flow coefficient than the thick IBL condition, and the size of the rotating stall cell increased with the increase of IBL thickness. Furthermore, Chen *et al.* (2012) have experimentally found that the IBL thickness has a great influence on the secondary flow in the cascade passage, especially near the corner. Li *et al.* (2016) explored the formation of the endwall boundary layer and its influence on the stage matching in a multi-stage compressor. By using the end-bend blade in a rear stage, the development of the endwall boundary layer was modified and the matching between stages was improved. In addition, for conventional cascades, the positive relationship between the incidence angle and the corner separation loss seems to be an uncontroversial fact. The numerical calculation results of Gbadebo *et al.* (2005) showed that when the incidence angle was negative, there was no critical separation point in the separation zone of suction surface. When incidence angle was above 0° , with the increase of incidence

angle, the separation line from the separation critical point continued to expand to the high-span area and the middle area of endwall, and finally increased the loss. Through oil flow experiment and numerical simulation, *Lewin et al. (2010)* found that before and after the development of corner stall, a small increase of the incidence angle would lead to reverse-flow increase substantially and a substantial increase in loss.

In practical applications, the tandem blades row is generally located at the rear stage of multi-stage compressors. Thus, the endwall boundary layer is formed and gradually thickens in the front stages, having a great impact on the later stages. This illustrates the practical significance of considering IBL in the analysis of tandem cascade. As a matter of fact, large attention has been paid to optimization, and numerical and experimental works have been done on the tandem cascade performance with nearly uniform inlet axial velocity profile. However, to the authors' knowledge, fewer works have reported so far to clarify how the IBL affects tandem cascade flow at different operating points. In order to properly understand the influence of the IBL thickness on the aerodynamic performance of tandem blades, we here focus on the flow field characteristics in tandem cascade under different incidence angles and IBL thickness, and their impact on the aerodynamic performance will be analyzed as well.

2. PHYSICAL MODEL AND NUMERICAL METHOD

2.1 Cascade Models

In this paper, a low aspect ratio high subsonic compressor cascade was selected as the original cascade. Table 1 presents the main design parameters of the original cascade, whose camber angle is 48° . The Reynolds number based on inlet velocity and blade chord is 5.6×10^5 at the design condition.

Under the assumption that design parameters of the original cascade remained unchanged, the blade profile has been designed with tandem layout. The

five geometric parameters of the tandem cascade are shown in Table 2, and have been chosen according to the conclusions of previous literature (*McGlumphy et al. 2009; McGlumphy et al. 2010*) to improve performance. Among them, AO is the axial overlap, PP is the percent pitch, CR is the chord ratio, TR is the camber ratio, and KBB is the approximate incidence angle of the RB. Additionally, d_a is axial distance between the FB trailing edge and the RB leading edge, and t is pitchwise distance between the FB trailing edge and the another RB leading edge. β_{11} and β_{12} are FB design inflow and outflow angles. β_{21} and β_{22} are RB design inflow and outflow angles. Figure 2 displays the two-dimensional blade profile and three-dimensional straight blade of the original cascade and tandem cascade.

Table 1 Main design parameters of the original cascade

Parameter	Value
Chord C /(mm)	40
Blade span h /(mm)	40
Blade pitch S /(mm)	22
Aspect ratio h/C	1
Blade solidity C/S	1.82
Stagger angle β_s /(degree)	22.5
Inflow angle β_1 /(degree)	42
Turning angle $\Delta\beta$ /(degree)	42
Inlet Mach number Ma_1	0.67

Table 2 Geometric parameters of the tandem cascade

Parameter	Definition	Value
AO	d_a/C_a	0
PP	t/S	0.9
TR	$(\beta_{21} - \beta_{22}) / (\beta_{11} - \beta_{12})$	2.3
CR	C_{RB}/C_{FB}	1
KBB	$\beta_{12} - \beta_{21}$ /(degree)	-6

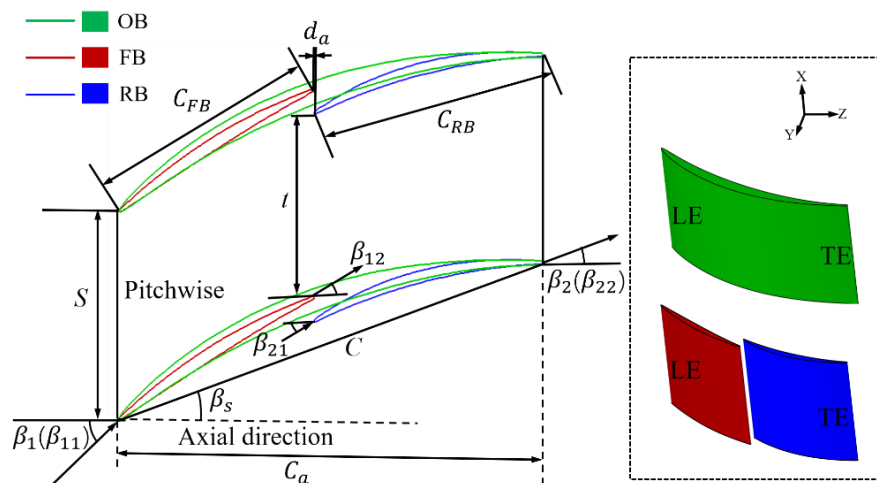


Fig. 2. Two-dimensional blade profile and three-dimensional straight blade of the original cascade and the tandem cascade.

2.2 Numerical Methodology

The numerical simulations in this paper have been conducted by using the commercial computational fluid dynamics software ANSYS CFX to solve the 3D steady Reynolds averaged Navier–Stokes equations. SST $k-\omega$ turbulence model was used to simulate the turbulent phenomena, which is suitable for the simulations of full development turbulence and near-wall turbulence. The model also allows us to consider the influence of the transport of shear stress on the turbulence viscosity coefficient, effectively avoiding overestimation of eddy-viscosity coefficient. We estimate that the separation flow at the adverse pressure gradient can be predicted with high accuracy.

Figure 3 shows the computational domain of the tandem cascade, which is a single blade passage. Periodic boundary conditions were applied in the circumferential direction of the cascade as a translational extension. The blade and endwall were assumed adiabatic and non-slip. In parallel, due to the spanwise flow symmetry of the cascade, symmetrical boundary conditions were used at the position of the 50% h , and only half of the blade height was simulated to reduce the cost of numerical computation. The inlet boundary of the computational domain was set to 0.8 times of the axial chord length (C_a) away from the blade leading edge, and the outlet was set to $2.5C_a$ away from the blade trailing edge. In the numerical simulation, the total pressure distribution, total temperature (311.7K), turbulence intensity (4%), turbulence length scale (0.004m) and flow direction were given at the inlet, and the static pressure was adjusted at the outlet to ensure that the inlet Mach number is 0.67.

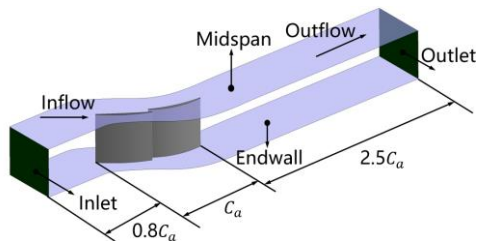


Fig. 3. Computational domain of the tandem cascade.

According to the cascade parameters, three different IBL thicknesses conditions (0mm, 2mm and 5mm) were considered, and the ratios of their relative blade heights are 0%, 5% and 12.5% respectively. They will be referred to as No-IBL, Thin-IBL and Thick-IBL respectively. The total pressure distribution of the three IBL thickness conditions is shown in Fig. 4.

The computational domain grid was automatically generated by the *Autogrid5* (2009) module of the NUMECA software. The tandem cascade grid was formed by the periodic matching connection of the O4H topology grids of the FB and RB, which ensures that the grid orthogonality is greater than 10° , the grid aspect ratio is less than 2000 and the grid

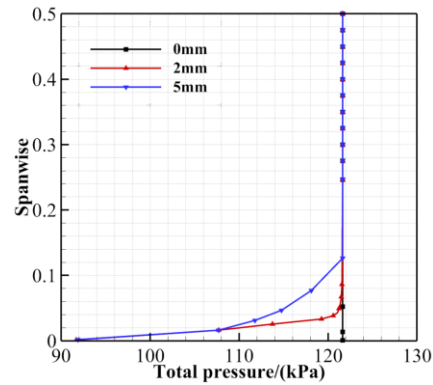


Fig. 4. Inlet flow total pressure distribution.

expansion ratio is less than 5. In order to meet the requirement of the SST $k-\omega$ turbulence model that the y^+ value near the wall is less than 1, the surface mesh of the blade and the endwall were locally refined. Figure 5 displays the grid of the endwall and the suction surface of the tandem cascade. It also contains an enlarged view of the partial mesh at the leading edge, the trailing edge and the gap between the FB and RB. The default O4H topology includes skin block (O-mesh), inlet block (H-mesh), outlet block (H-mesh), up block (H-mesh) and down block(H-mesh), which are surrounding the blade, located upstream the leading edge (LE), located downstream the trailing edge (TE), located above the blade section and located above the blade section, respectively.

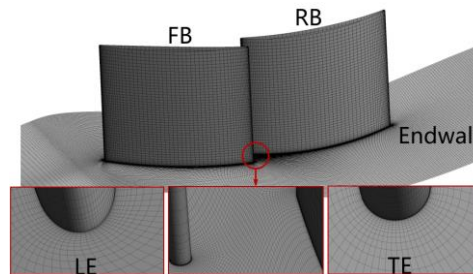


Fig. 5. Overall and partial meshes of the tandem cascade.

To verify the grid independence, the inlet Mach number (Ma_1) and the outlet total pressure loss coefficient (ω) of the tandem cascade with different grid numbers are illustrated in Fig. 6. A distance of $140\%C_a$ from leading edge is defined as the outlet measurement position, which is the real outlet in this paper. Equation (1) contains the definition of the total pressure loss coefficient. The inlet total pressure, inlet static pressure and local total pressure are denoted by P_{t1} , p_1 and P_t respectively.

$$\omega = \frac{P_{t1} - P_t}{P_{t1} - p_1} \quad (1)$$

As it may be seen in Fig. 6, the simulation results for the tandem cascade tend to be converged when its grid number exceeds 2.55 million, eliminating the influence of the grid number on the simulation

results. As a consequence, the total grid number of tandem cascades is finally set to 2.97 million, in order to balance the computational cost and the accuracy.

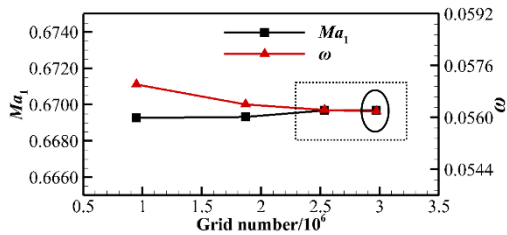


Fig. 6. Grid independence validation of the tandem cascade.

In order to further verifying the accuracy of the numerical methods, the results of the original cascade have been experimentally verified. Figure 7 presents the distributions of pitch-averaged total pressure loss coefficient and outlet flow angle in spanwise (Liesner *et al.* 2010). We may observe that the numerically simulated outlet airflow angle is in good agreement with the experimental results, but the total pressure loss coefficient is different in the endwall region, which is a common feature, present also in previous studies (Liesner *et al.* 2010; Chen *et al.* 2014). A remarkable feature of Fig. 8 is that the numerical simulations predict very well the corner separation range of the suction surface, as well as the development of the secondary flow, which further verifies the reliability of the numerical methods used in this paper (Meyer *et al.* 2003).

3. RESULTS AND DISCUSSION

3.1 Comparison of the Aerodynamic Performance between the Original Cascade and the Tandem Cascade

In this section, an overview about the results at outlet is presented to compare the difference in the aerodynamic performance of the original cascade and the tandem cascade under design condition. The cascade performance under different IBL thicknesses is shown in Table 3 and Table 4. The static pressure rise coefficient (C_p) is defined as

$$C_p = \frac{p - p_1}{P_{t1} - p_1} \quad (2)$$

The inlet total pressure and static pressure are denoted by P_{t1} and p_1 respectively, and the local pressure is denoted by p .

It can be seen that the total pressure loss coefficient of the original cascade and tandem cascade increases with the increase of the IBL thickness, while the static pressure rise coefficient behaves in an opposite way. In general, compared with the original cascade, the tandem cascade can effectively reduce the total pressure loss and improve the static pressure rise. However, the increase of the IBL thickness degrades

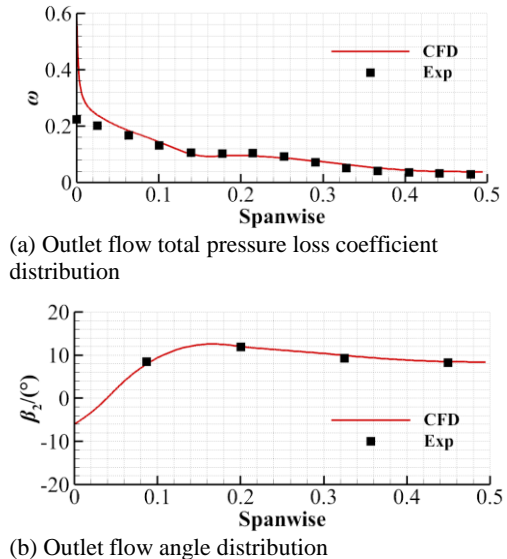


Fig. 7. Comparison between the numerical and experimental results of the original cascade.

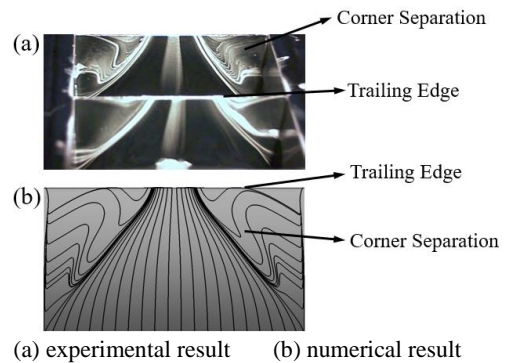


Fig. 8. Comparison of numerical and experimental results of the flow patterns on the blade suction surface.

Table 3 Total pressure loss coefficient of two cascades

IBL thickness	Original cascade	Tandem cascade
0mm	0.06324	0.05621 (-11.1%)
2mm	0.08142	0.07692 (-5.5%)
5mm	0.10293	0.09877 (-4.1%)

Table 4 Static pressure rise coefficient of two cascades

IBL thickness	Original cascade	Tandem cascade
0mm	0.41210	0.44241 (+7.4%)
2mm	0.39869	0.42468 (+6.5%)
5mm	0.37228	0.39814 (+6.4%)

the advantage of tandem cascade. A comparison of the flow characteristics between the original and the tandem cascade can be found in (Mao *et al.* 2022).

3.2 Flow Characteristics and Aerodynamic Performance under Different Incidence Angles (No-IBL)

In order to analyze the influence of incidence angle on the flow characteristics of the tandem cascade, three incidence angles of -2° , 0° , and 4° were investigated for an IBL thickness is of $0\%h$ (No-IBL). Figure 9 depicts the Mach number (Ma) and total pressure loss coefficient (ω) contours at $5\%h$ plane under different incidence angles. Additionally, the partial surface streamlines are marked in Fig. 9. It is noticeable that as the incidence angle increases, the separation range near the FB trailing edge becomes larger, and the corresponding total pressure loss increases.

Figure 9 clearly shows that there is a high-momentum fluid in the passage between the pressure surface of the FB trailing edge and the suction surface of the RB leading edge, which is referred to as "gap flow". The gap flow can effectively weaken the mixing of FB and RB wakes near the RB trailing edge. As the incidence angle increases, the momentum of the gap flow decreases. At the same time, due to the low-energy fluid of the FB wake increases, the mixing of FB wake and RB wake gets stronger at the 4° incidence angle, resulting in more low-energy fluid accumulating near the RB trailing edge and a larger range of high loss. Besides, although there is less low-energy fluid around the RB trailing edge at the -2° incidence angle than the 4° incidence angle, the loss caused by the separation of the boundary layer on the suction surface becomes higher.

The distributions of C_p of the blade surface at $5\%h$

and $50\%h$ along the normalized axial chord under different incidence angles are shown in Fig.10. One can see that the C_p distributions of FB changes significantly for the incidence angle changing from negative to positive values, with the greatest values at the trailing edge for the positive incidence angle. On the other hand, the C_p distributions of RB at different incidence angles are similar, although the loads are different. Moreover, at $5\%h$, as the incidence angle increases, the load of the FB increases and the flow separation becomes more serious, as it can be seen from Fig. 9 (a). The FB wake accumulates in the blade passage, and the blade passage blockage weakens the pressure diffusion capacity of RB. As a result, this reduces the axial adverse pressure gradient and load, thus making the RB trailing wake loss decreases. This is consistent with the analysis of Fig. 9. Finally, at $50\%h$, the C_p distributions of FB are similar to that at $5\%h$. Meanwhile, at $5\%h$, the C_p distributions of RB are different from that at the mainstream area ($50\%h$) because of serious passage blockage.

Figure 11 presents the Q isosurface and axial vorticity contours for different incidence angles. The Q isosurface refers to the turbulent kinetic energy and is used to analyze the structure, scale and evolution of the vortex in the tandem cascade passage. As a vortex determination criterion, Q reflects a balance between the rotation and deformation of fluid micelle in the flow field, with $Q > 0$ indicating that the rotational motion of fluid micelle is dominant. To analyze the RB corner separation in detail, we select two axial observation sections, denoted by Plane1 and Plane2 respectively, where the positions are $85\%C_a$ and $140\%C_a$ from leading edge. The axial vorticity contours corresponding to the two sections are also shown in Fig. 11.

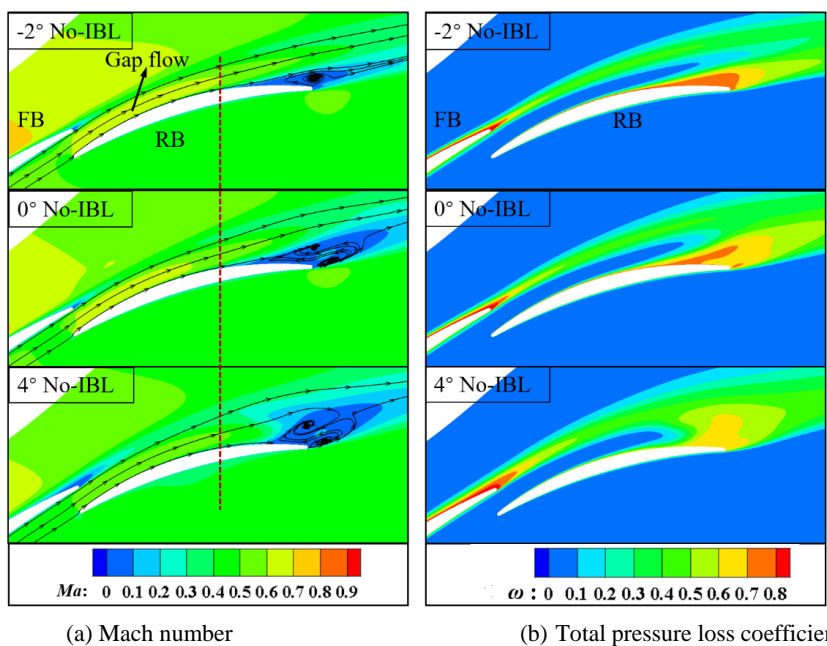


Fig. 9. Mach number and total pressure loss coefficient contours at $5\%h$ plane for tandem cascade under different incidence angles, No-IBL.

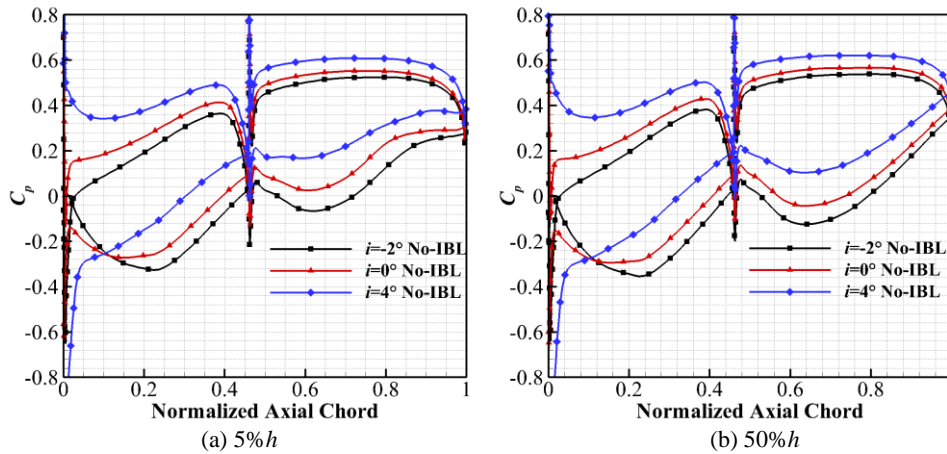


Fig. 10. C_p distributions of the tandem cascade, No-IBL.

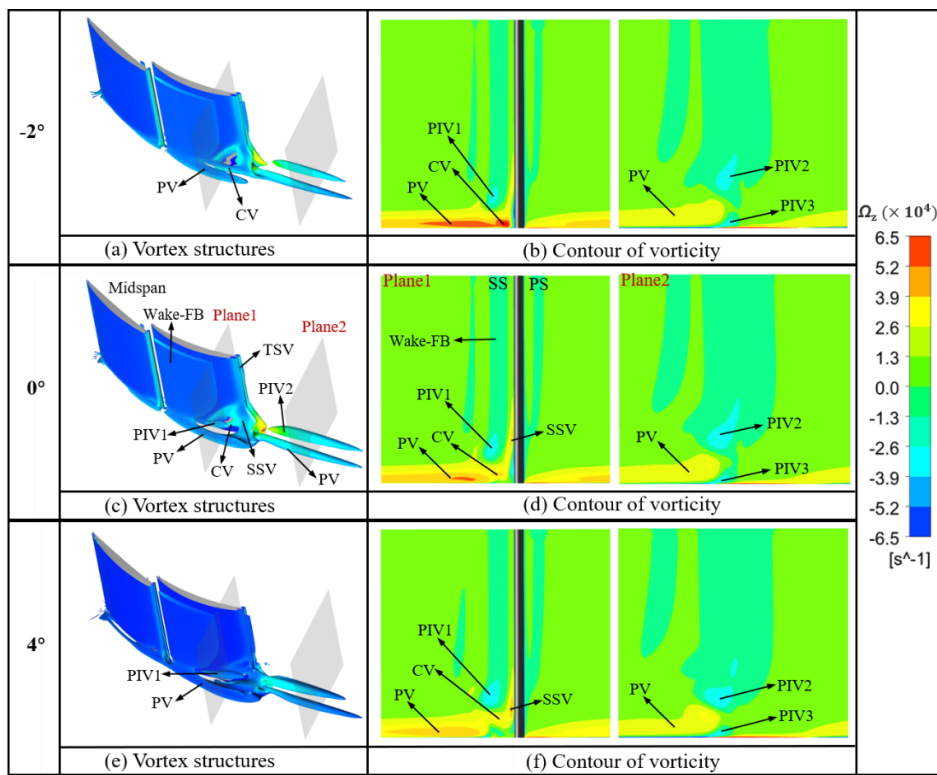


Fig. 11. Q isosurface contours and axial vorticity contours of the tandem cascade under different incidence angles, $Q = 8 \times 10^7 \text{ s}^{-2}$, No-IBL.

In order to observe the FB corner separation phenomenon more clearly, we show the axial vorticity contours at the 94% forward blade C_a position in Fig. 12. It can be seen that the FB vortex structure is relatively simple, and only passage vortex (PV) are present. When the incidence angle changes from -2° to 0° , the portion of PV scale near the suction side slightly increases, whereas the other portion of PV scale, near the pressure side slightly decreases. Upon further increasing the incidence angle to 4° , the PV scale increases significantly. Overall, the behaviour of FB corner separation as a function of the incidence angle is similar to that of the conventional single blade.

Next, the RB vortex structure is analyzed in detail. The behaviour at 0° incidence angle is shown in Fig. 11 (c), where one can see that there is a large wake vortex near the RB suction surface. This is formed by the shearing of the low-momentum fluid in the FB wake and the high-momentum fluid in the gap flow, and it is denoted by Wake-FB. PV in the RB passage is promoted by the circumferential flow of the low-energy fluid at the endwall, and develops along the flow direction in the form of a quasi-cylindrical vortex. Affected by the wake near the FB endwall, the scale of the PV structure is larger, and it gradually moves away from the suction surface due to the squeezing effect of the gap flow in the downstream

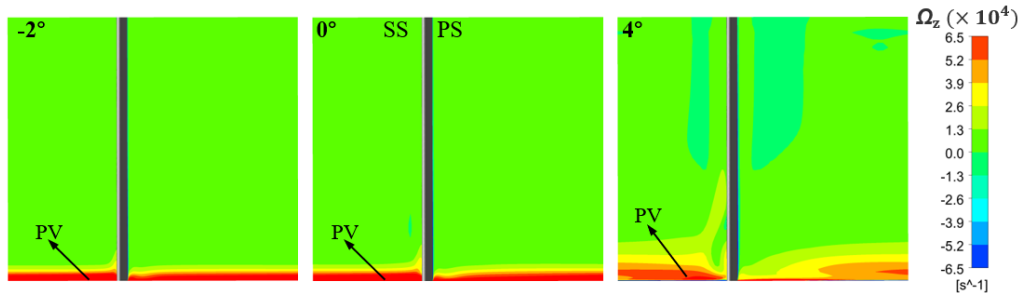


Fig. 12. FB axial vorticity contours of the tandem cascade under different incidence angles, No-IBL

development process. From Fig. 13, which is partially enlarged view of Fig. 11 (c), one can see that near the suction surface and the endwall, there is a corner vortex (CV) formed by the interaction of the gap flow and the endwall low-energy fluid. This CV is marked with red dotted line in Fig. 13. It interacts and mixes with the layered suction surface separation vortex (SSV), trailing-edge shedding vortex (TSV) and PV at the position near the RB trailing edge to form a columnar vortex at the cascade passage exit. Since PV provides the most relevant contribution, this columnar vortex is still named PV in this paper. There is another columnar vortex above the PV at Plane1, and it can be seen from Fig. 11 (d) that this vortex is actually a part of Wake-FB. However, it is close to PV and CV, and its vorticity is smaller than PV and CV. Meanwhile, it is opposite to their rotation direction, so we suggest that this vortex is an induced vortex (PIV1) produced by the combined action of Wake-FB, PV and CV. Two another induced vortices (PIV2 and PIV3) of the PV can be observed looking at Plane2 in Fig. 11 (d).

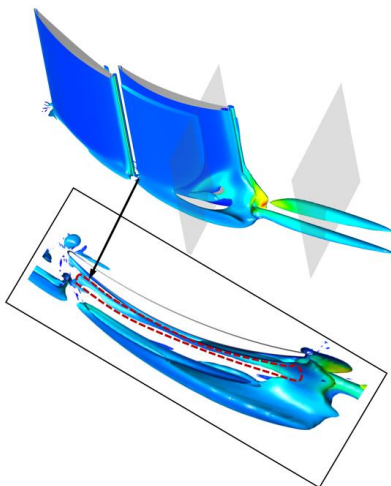


Fig. 13. Partial enlarged vertical view of the rear blade at 0° incidence angle.

When the incidence angle gradually increases from -2° to 4° , the PV vorticity at the corner region (Plane1) decreases due to the decrease of the RB load. The scale of the PIV1 vortex structure is increased, which indicates that PIV1 is mainly affected by Wake-FB. As it can be seen in Fig. 11 (b), when the incidence angle is -2° , the CV is near the endwall and the vorticity is large. With the

increment of incidence angle, the gap flow weakens, so the CV position gradually moves upward in the span direction and the vorticity is reduced, and it is mixed with SSV at the 4° incidence angle, which can be seen from Fig. 11 (f). On the contrary, the vorticity of PIV2 and PIV3 hardly change. Finally, as shown in Fig. 11 (e), PV mixes with other vortices the most near the RB trailing edge at the 4° incidence angle because of the weakest gap flow.

To quantitatively analyze the outlet loss, the distributions of mass pitch-averaged total pressure loss coefficient at outlet ($140\% C_a$ downstream of leading edge) under different incidence angles along the half-blade height are shown in Fig. 14. The outlet loss can be divided into the corner separation loss and the wake loss (near $50\%h$), which itself includes the blade profile loss and trailing edge mixing loss. It can be observed that the wake loss is highest at 4° incidence angle. As the incidence angle increases, the spanwise corner separation range increases and it is accompanied by higher loss. Additionally, it can be also observed that as the incidence angle increases, the loss in the range of $0\%h-8\%h$ gradually decreases which indicates that in Fig. 9, although the RB wake loss range at the 4° incidence angle is larger, its overall loss is less than that at the -2° incidence angle. At the same time, the behaviour of loss as a function of the incidence angle in the range of $8\%h-50\%h$ is opposite to that in the range of $0\%h-8\%h$. To explain this phenomenon, in Fig. 15 we depict the loss contours on multiple S3 sections under different incidence angles.

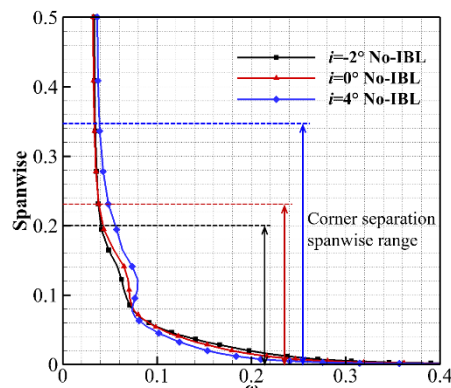


Fig. 14. Spanwise distribution of mass pitch-averaged total pressure loss coefficient at outlet, No-IBL.

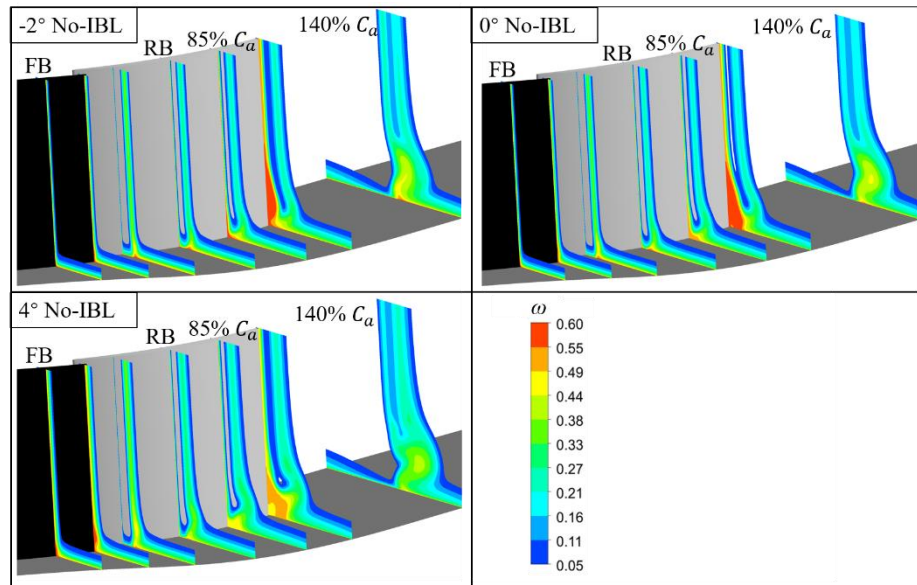


Fig. 15. Total pressure loss contours on multiple S3 sections, No-IBL.

One can see from Fig. 15 that in the mainstream area ($20\%h-50\%h$), the strength of the gap flow is sufficient to prevent the mixing of the FB and RB wakes. Meanwhile, as the incidence angle increases, the FB wake loss increases, and the RB wake loss decreases, hence the reason for the greatest outlet loss at the 4° incidence angle in the mainstream zone is mainly related to FB. Additionally, the weaker gap flow has a weaker inhibitory effect on the stronger FB wake at the 4° incidence angle, so the mixing effect between the FB wake and the RB secondary flow is stronger, which further makes the high-loss zone at $85\% C_a$ (Plane1) to increase in the circumferential direction. This is also consistent with the above analysis of the PV mixing with other vortices. Upon combining Fig. 11 and Fig. 15, one can see that the outlet loss near the endwall area ($0\%h-8\%h$) at the -2° incidence angle is the highest. This is because the strong vorticity of PV and CV produce a large loss. Finally, because the scale of the PIV2 vortex structure at outlet ($140\% C_a$ downstream of leading edge) increases with the incidence angle, the loss at the 4° incidence angle is the largest in the range of $8\%h-20\%h$.

3.3 Flow Characteristics and Aerodynamic Performance under Different Incidence Angles (Thick-IBL)

Figure 16 shows the total pressure loss contours at outlet ($140\% C_a$ downstream of leading edge) in different conditions (i.e. different IBL and values of the incidence angle). The aerodynamic performance of the tandem cascade is modified by the presence of IBL. It can be seen from Fig. 16 that different IBL conditions significantly affect the level and the range of the total pressure loss at the outlet, but the loss distributions in the Thin-IBL and Thick-IBL conditions are similar. Therefore, only the Thick-IBL condition is analyzed in detail in this section. Figure 17 shows the Mach number and total pressure loss coefficient contours at $5\%h$ plane for different

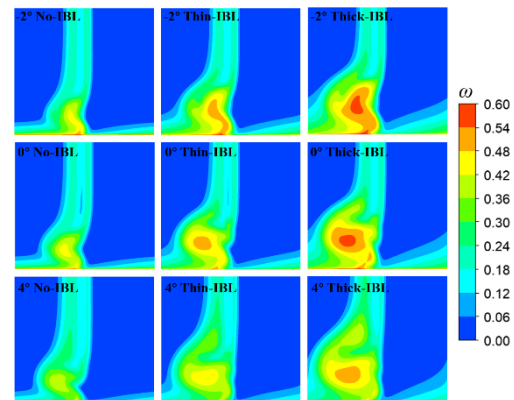


Fig. 16. Total pressure loss contours in different conditions.

incidence angles. Combining these results with those illustrated in Fig. 9, it is apparent that the behaviour of the FB wake loss, the RB wake loss and the gap flow strength with the incidence angle are the very similar to that observed in the No-IBL condition. However, at the same incidence angle, the FB wake loss at the Thick-IBL condition is higher than that at the No-IBL condition, while the RB wake loss is lower. Besides, due to the influence of IBL, the gap flow strength at $5\%h$ at the Thick-IBL condition is smaller than that at the No-IBL condition. As a whole, it can be concluded that at $5\%h$, the positive incidence angle and the thick IBL make the flow separation of FB more significant, a larger amount of low-energy fluid thus accumulates in the flow passage, which greatly reduces the diffusing capacity of RB and, in turn, leads to a smaller flow separation.

The C_p distributions of the blade surface at $5\%h$ and $50\%h$ under different incidence angles and IBL conditions are presented in Fig. 18. It should be pointed out that, for the convenience of comparative analysis, the aerodynamic parameter distributions at

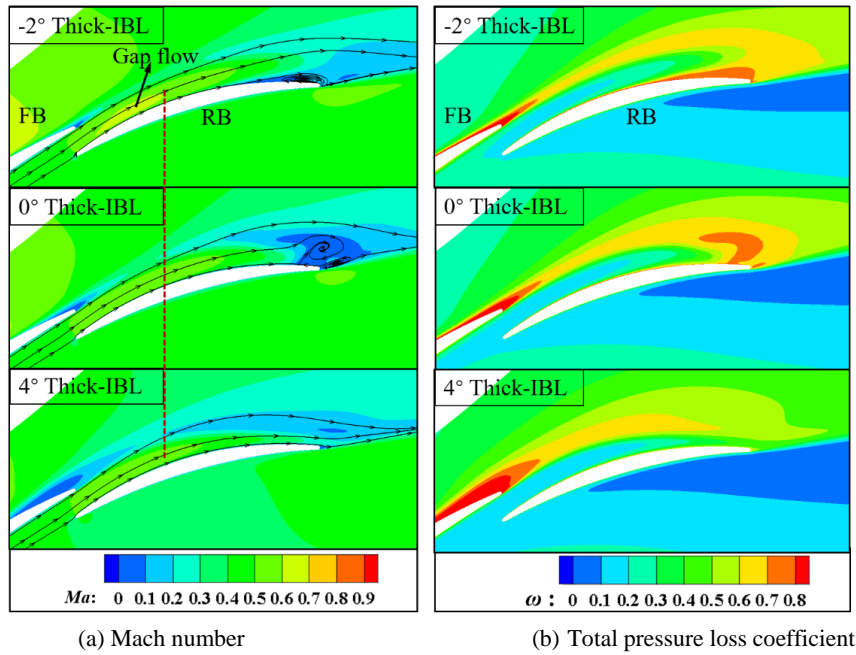


Fig. 17. Mach number and total pressure loss coefficient contours at 5%h plane for tandem cascade under different incidence angles, Thick-IBL.

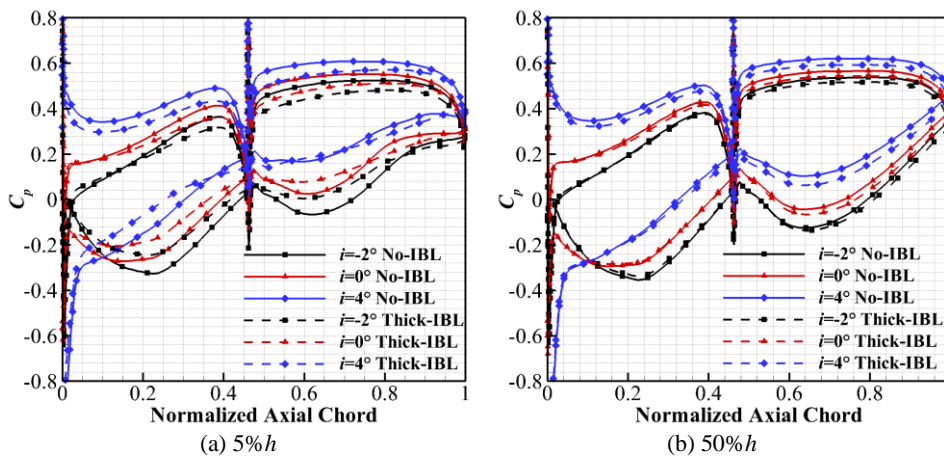


Fig. 18. C_p distributions of the tandem cascade.

the No-IBL condition of Fig. 10 is added to Fig. 18. Due to the existence of IBL, the low-energy fluid near the endwall increases and leads to the flow passage block, so that the FB load and the axial adverse pressure gradient decrease at the 5%h. Similarly, the blockage of the low-energy fluid in the FB passage causes the RB load at the 5%h to drop. At 50%h, the load of FB at the 4° incidence angle decreases with the IBL thickening, which indicates that the low-energy fluid from IBL near the endwall has a significant influence on the flow in the main flow area. Besides that, at 50% h, although the C_p distributions of RB are different for different IBL conditions, their loads are very similar.

Figure 19 depicts the Q isosurface contours and axial vorticity contours of the tandem cascade at Thick-IBL condition. The magnitude of the Q value and the positions of the two observation sections are the same as those used in Section 3.2. For all the

incidence angles, the thickening of IBL leads to the increase of the FB corner separation zone. This is due to the action of the axial pressure gradient and the circumferential pressure gradient, which cause a stronger endwall secondary flow in the blade passage. Combining the results reported in Fig. 11 and Fig. 19, one concludes that although the RB load decreases due to the existence of IBL, the PV scale still increases, such that the vorticity and structure scale of PIV1, PIV2 and PIV3 increase. Thus, the high loss range at the outlet expands along the spanwise and circumferential direction as IBL thickens (see Fig. 16). Furthermore, since the presence of IBL reduces the gap flow strength near the endwall, the vorticity of the CV decreases, but this does not suppress the increasing trend of total loss.

Figure 20 illustrates the distributions of mass pitch-averaged total pressure loss coefficient at the outlet

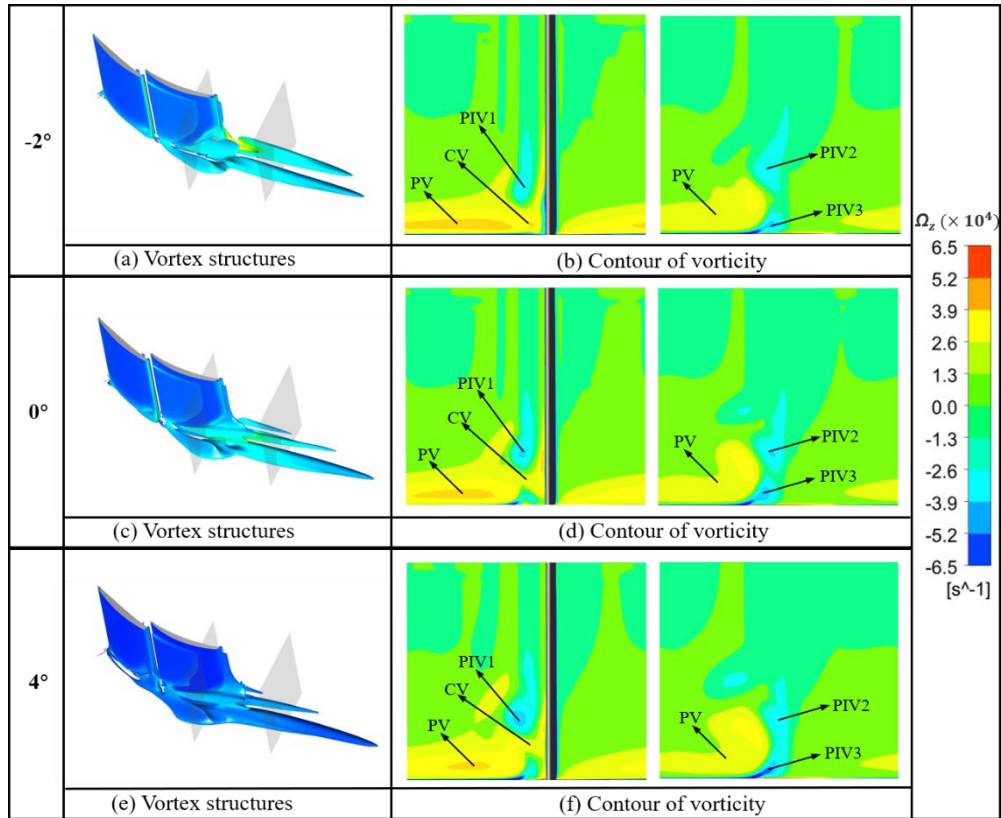


Fig. 19. Q isosurface contours and axial vorticity contours of the tandem cascade under different incidence angles, $Q = 8 \times 10^7 \text{ s}^{-2}$, Thick-IBL.

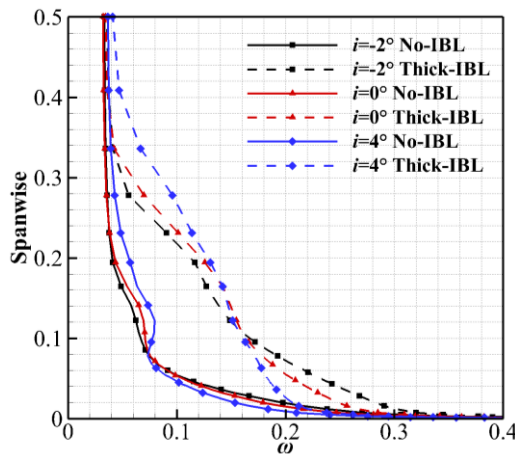


Fig. 20. Spanwise distribution of mass pitch-averaged total pressure loss coefficient at outlet.

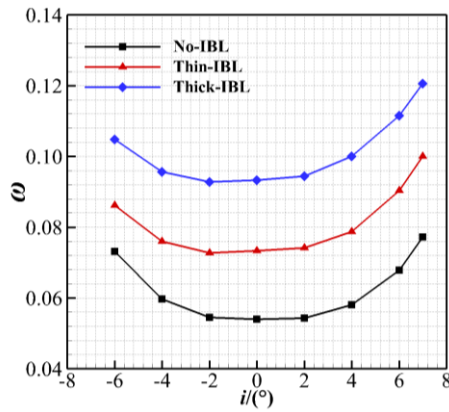
($140\% C_a$ downstream of leading edge). At Thick-IBL condition, the outlet loss distributions for all incidence angles are similar to that at No-IBL condition. However, the increase of IBL thickness makes the loss at the Thick-IBL condition larger than the No-IBL case, in nearly the whole spanwise range, and in the mainstream area near the $50\%h$. The change of total pressure loss is small except that for 4° incidence angle condition, because the total pressure loss in this area is mainly due to the blade profile loss and trailing edge mixing loss, which are only little affected by the endwall IBL.

3.4 Total Aerodynamic Performance Analysis

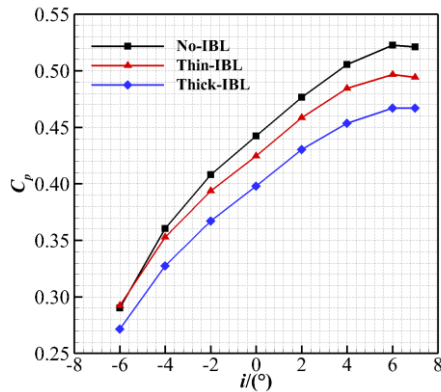
Figure 21 shows the variation of the total pressure loss coefficient and static pressure rise coefficient with the incidence angle under different IBL thickness, and the parameter differences compared with No-IBL condition are presented in Table 5 and Table 6. It can be observed that as the IBL thickness increases, the loss at all incidence angles increases to varying degrees, and the C_p decreases to different extent, except for -6° incidence angle. It's interesting to observe that the presence of IBL changes the minimum loss condition from 0° (design condition) to -2° incidence angle. Furthermore, for Thin-IBL and Thick-IBL conditions, as incidence angle increases, the loss increment increases continuously within the $-6^\circ \sim 2^\circ$ incidence angles, and decreases within the $2^\circ \sim 7^\circ$ incidence angles. This means that the maximum loss increment is at 2° incidence angle. In terms of the static pressure rise coefficient, the maximum decrement value is found at 6° incidence angle (Thick-IBL condition) or at 7° incidence angle (Thin-IBL condition).

4. CONCLUSION

In this paper, the influence of inflow conditions (incidence angle and IBL thickness) on the 3D flow field structure and aerodynamic performance of a tandem cascade has been investigated numerically.



(a) Total pressure loss coefficient



(b) Static pressure rise coefficient

Fig. 21. Overall aerodynamic performance in the available incidence angle range under different IBL thicknesses.

Table 5 Total pressure loss coefficient difference

i	No-IBL	Thin-IBL	Thick-IBL
-6°	–	+17.9%	+43.3%
-4°	–	+27.2%	+60.2%
-2°	–	+33.5%	+70.4%
0°	–	+36.0%	+72.9%
2°	–	+36.4%	+73.8%
4°	–	+35.7%	+72.4%
6°	–	+33.1%	+64.4%
7°	–	+29.6%	+56.1%

Table 6 Static pressure rise coefficient difference

i	No-IBL	Thin-IBL	Thick-IBL
-6°	–	+0.7%	-6.4%
-4°	–	-2.1%	-9.1%
-2°	–	-3.5%	-9.9%
0°	–	-4.0%	-10.0%
2°	–	-3.8%	-9.7%
4°	–	-4.2%	-10.3%
6°	–	-5.0%	-10.6%
7°	–	-5.2%	-10.4%

The main conclusions of our analysis can be summarized as follows:

(1) The gap flow strength between FB and RB of the tandem cascade decreases with the increase of the incidence angle. The gap flow can effectively reduce the wake mixing of FB and RB in the main flow region, and can prevent the PV in the RB passage from developing along the circumferential direction.

(2) In the RB passage of the tandem cascade, in addition to the conventional vortices such as SSV, TSV and PV vortices, there are also CV formed by the interaction between the gap flow and the low-energy fluid near the endwall. Three further induced vortices of PIV1, PIV2 and PIV3 related with PV can be observed as well.

(3) For both the No-IBL and Thick-IBL conditions, the maximum outlet loss condition of the tandem cascade is -2° incidence angle in the range of 0%h-8%h (No-IBL) or 0%h-10%h (Thick-IBL). This is related to the existence of PV and CV with strong vorticity. However, in other ranges, the maximum is found at 4° incidence angle, and this is related to the larger FB wake loss.

(4) The existence of the IBL does not change the influence characteristics of the incidence angle on the tandem cascade. On the other hand, it reduces the RB load and the gap flow strength near the endwall. Moreover, the IBL aggravates the FB 3D corner separation and increases the vorticity and structural scale of PV, PIV1, PIV2 and PIV3 of the RB. It also reduces the vorticity of the CV.

(5) For different incidence angles, the IBL increases the loss of the tandem cascade and decrease the static pressure rise (except for -6° incidence angle). The maximum loss increment is at 2° incidence angle, and the maximum static pressure rise decrement is at 6° incidence angle (Thick-IBL condition) or at 7° incidence angle (Thin-IBL condition). Furthermore, the presence of IBL changes the minimum loss condition from 0° (design condition) to -2° incidence angle.

The current study indicates that the presence of IBL reduces the tandem cascade two-dimensional performance advantage compared to the conventional cascade and worsens the tandem cascade performance within the full incidence angle range. The ongoing studies will attempt to address the above issues through 3D blade optimization and endwall suction schemes. On the one hand, the forward and rear blade profiles of the tandem cascade near the endwall and the five parameters in the Table 2 should be optimized. On the other hand, grooved suction will apply to the tandem cascade endwall to reduce the endwall secondary flow effect, and to better utilize the tandem cascade two-dimensional performance advantage.

ACKNOWLEDGMENTS

This paper is supported by the National Science and Technology Major Project under Grant 2017- II - 0001-0013, Fundamental Research Funds for the

Central Universities under Grant D5000210483, Funds of National Key Laboratory of Science and Technology on Aerodynamic Design and Research under Grant D5150210006 and the National Natural Science Foundation of China under Grant 51790512 and 52106057. These supports are gratefully acknowledged. Additionally, we would like to express our gratitude to EditSprings for the expert linguistic services provided.

REFERENCES

- AutoGrid5 v8.7, User Manual (2009). Brussels: NUMECA International.
- Bammert, K. and R. Staude (1980). Optimization for rotor blades of tandem design for axial flow compressors. *Journal of Engineering for Gas Turbines and Power* 102(2), 369-375.
- Cao, Z., W. Guo, C. Song and B. Liu (2021). Flow physics of highly loaded tandem compressor cascade with non-axisymmetric endwall profiling. *Proceedings of the Institution of Mechanical Engineers, Part A: Journal of Power and Energy* 235(5), 931-943.
- Chen, P., K. Liesner, R. Meyer and W. Qiao (2012). Effect of inflow variations on compressor secondary flow behavior. *XX Polish Fluid Mechanics Conference*, Gliwice.
- Chen, P., W. Qiao, K. Liesner and R. Meyer (2014). Location effect of boundary layer suction on compressor hub-corner separation *Turbo Expo: Power for Land, Sea, and Air*, GT 2014-25043.
- Cheng, H., B. Liu, J. Li and X. Yang (2017). A study of parameter optimization of axial compressor tandem cascade. *Journal of Propulsion Technology* 38(10), 2224-2234.
- Choi, M., H. T. Chung, S. H. Oh, H. Y. Ko and J. H. Baek (2011). Effects of inlet boundary layer thickness on characteristics of rotating stall in subsonic axial compressor. *Transactions of the Japan Society for Aeronautical and Space Sciences* 53(182), 267-274.
- Eshraghi, H., M. Boroomand and A. M. Tousi (2016). A developed methodology in design of highly loaded tandem axial flow compressor stage. *Journal of Applied Fluid Mechanics* 9(1), 83-94.
- Gbadebo, S. A., N. A. Cumpsty and T. P. Hynes (2005). Three-dimensional separations in axial compressors. *Journal of Turbomachinery* 127(4), 331-339.
- Hertel, C., C. Bode, D. Kožulović and T. Schneider (2014, June). Investigations on aerodynamic loading limits of subsonic compressor tandem cascades: end wall flow. *Turbo Expo: Power for Land, Sea, and Air*, GT2014-26978.
- Hoeger, M., R. D. Baier, S. Fischer and J. Neudorfer (2011, July). High turning compressor tandem cascade for high subsonic flows, part 1: Aerodynamic design. *47th AIAA/ASME/SAE/ASEE Joint Propulsion Conference & Exhibit*, 5601.
- Ju, Y. and C. Zhang (2010, October). Multi-objective optimization design method for tandem compressor cascade at design and off design conditions. *Turbo Expo: Power for Land, Sea, and Air*, 44021, 785-796.
- Lewin, E., D. Kožulović and U. Stark (2010, October). Experimental and numerical analysis of hub-corner stall in compressor cascades. *Turbo Expo: Power for Land, Sea, and Air*, 44021, 289-299.
- Li, Z., X. Zheng, Y. Liu, Q. Li and B. Ji (2016). The effect of end wall boundary layer on matching and corresponding flow control technique for multistage axial compressor. *Proceedings of the Institution of Mechanical Engineers, Part G: Journal of Aerospace Engineering* 230(12), 2179-2194.
- Liesner, K., R. Meyer, M. Lemke, C. Gmelin and F. Thiele (2010, October). On the efficiency of secondary flow suction in a compressor cascade. *Turbo Expo: Power for Land, Sea, and Air*, 44021, 151-160.
- Liu, B., C. Zhang, G. An, D. Fu and X. Yu (2021). Using tandem blades to break loading limit of highly loaded axial compressors. *Chinese Journal of Aeronautics* 35(4), 165-175.
- Mao, X., B. Liu and F. Yuan (2018). Numerical and experimental study of separation control by boundary layer aspiration in a highly-loaded axial compressor cascade. *Journal of Applied Fluid Mechanics* 11(2), 433-446.
- Mao, X., Z. Yang, B. Liu, B. Zhang and H. Wang (2022). Effects of inlet boundary layer on aerodynamic performance of tandem cascade. *Journal of Propulsion Technology*. doi:10.13675/j.cnki.tjjs.210738. [Chinese].
- McGlumphy, J. (2008). *Numerical investigation of subsonic axial-flow tandem airfoils for a core compressor rotor*. Ph.D. thesis, Virginia Polytechnic Institute.
- McGlumphy, J., W. F. Ng, S. R. Wellborn and S. Kempf (2009). Numerical investigation of tandem airfoils for subsonic axial-flow compressor blades. *Journal of Turbomachinery*, 131, 021018.
- McGlumphy, J., W. F. Ng, S. R. Wellborn and S. Kempf (2010). 3D numerical investigation of tandem airfoils for a core compressor rotor. *Journal of Turbomachinery* 132, 031009.
- Meyer, R., D. W. Bechert and W. Hage (2003, March). Secondary flow control on compressor blades to improve the performance of axial turbomachines. *In Proceedings 5th European Conference on Turbomachinery, Prag, Tschechische Republik*.
- Roy, B., A. Mulmule and S. Puranam (2009). Aerodynamic design of a part-span tandem

- bladed rotor for low speed axial compressor. *27th AIAA Applied Aerodynamics Conference* 3964.
- Schlaps, R. C., S. Shahpar and V. Gümmer (2014, June). Automatic three-dimensional optimisation of a modern tandem compressor vane. *Turbo Expo: Power for Land, Sea, and Air*, GT2014-26762.
- Song, Z., B. Liu and H. Cheng (2019). Adaptive particle swarm optimization with population diversity control and its application in tandem blade optimization. *Proceedings of the Institution of Mechanical Engineers, Part C: Journal of Mechanical Engineering Science* 233(6), 1859-1875.
- Tesch, A., M. Lange, K. Vogeler, J. Ortmanns, E. Johann and V. Gümmer (2014, June). An experimental investigation of a tandem stator flow characteristic in a low speed axial research compressor. *Turbo Expo: Power for Land, Sea, and Air*, GT2014-26104.
- Wagner, J. H., R. P. Dring and H. D. Joslyn (1985a). Inlet boundary layer effects in an axial compressor rotor: part I—blade-to-blade effects. *Journal of Engineering for Gas Turbines and Power* 107(2), 374-380.
- Wagner, J. H., R. P. Dring and H. D. Joslyn (1985b). Inlet boundary layer effects in an axial compressor rotor: part II—throughflow effects. *Journal of Engineering for Gas Turbines and Power* 107(2), 381-386.
- Wang, H., B. Liu and B. Zhang (2020). Passive control with blade-end slots and whole-span slot in a large camber compressor cascade. *Journal of Applied Fluid Mechanics* 14(3), 703-714.
- Wennerstrom, A. J. (1990). Highly loaded axial flow compressors: history and current developments. *Journal of Turbomachinery* 112(4), 567-578.
- Zhang, L., S. Wang and W. Zhu (2019). Application of endwall contouring in a high-subsonic tandem cascade with endwall boundary layer suction. *Aerospace Science and Technology* 84, 245-256.